

Combining Computational and Experimental Evidence for the Charge State of Oxygen Vacancies in ZrO_{2-x}

Claudio Imperato¹, Marzia Fantauzzi², Cristiana Passiu³, Ilaria Rea⁴, Chiara Ricca⁵, Ulrich Aschauer⁵, Filomena Sannino⁶, Gerardino D'Errico⁷, Luca De Stefano^{4*}, Antonella Rossi^{2,3*}, Antonio Aronne^{1*}

¹ *Dipartimento di Ingegneria Chimica, dei Materiali e della Produzione Industriale, Università di Napoli Federico II, Napoli, Italy.*

² *Dipartimento di Scienze Chimiche e Geologiche, Università di Cagliari, Cagliari, Italy.*

³ *Department of Materials, ETH Zurich, Zürich, Switzerland.*

⁴ *Istituto per la Microelettronica e Microsistemi, Consiglio Nazionale delle Ricerche, Napoli, Italy.*

⁵ *Departement für Chemie und Biochemie, Universität Bern, Bern, Switzerland.*

⁶ *Dipartimento di Agraria, Università di Napoli Federico II, Portici (Napoli), Italy.*

⁷ *Dipartimento di Scienze Chimiche, Università di Napoli Federico II, Napoli, Italy.*

The functional properties of metal oxide semiconductors depend on intrinsic and extrinsic defects. The population of intrinsic defects is strongly affected by the synthesis method and treatments the material is subjected to, while extrinsic defects can originate from suitable doping. Stoichiometric ZrO_2 is a non-reducible oxide with a large band gap. Therefore, controlling and modulating its defect profile to induce states in the band gap is the sole possibility to make it a photocatalyst responsive to visible light. We report a method, based on low temperature synthesis coupled with treatments performed in mild conditions, to obtain visible light photoresponsive ZrO_{2-x} . The electronic structure of these materials is interpreted in relation to their oxygen vacancy defect population. On the basis of a wide set of experimental measurements and supported by theoretical calculations, we demonstrate, for the first time, the predominance of positively charged F-center oxygen vacancies that do not give rise to Zr^{3+} species.

Zirconium oxide (ZrO_2) occurs in three polymorphs: the monoclinic structure is thermodynamically stable at room temperature and reversibly transforms to the tetragonal polymorph (T- ZrO_2) at 1150 °C, whereas the cubic phase is stable at temperatures in excess of 2370 °C¹. Despite its large band gap (E_g) characterized by two direct transitions at 5.2 and 5.79 eV², ZrO_2 was recently proposed as a photocatalyst³⁻⁵. The visible-light photoresponsivity of zirconia-based materials was obtained either by doping with rare-earth metals, such as Ce^3 and Er^4 , using wet synthesis methods, or by magnesiothermic reduction of commercial monoclinic ZrO_2 ⁵. Oxygen vacancies are the main intrinsic defects in ZrO_2 and they play a key role in defining its functional and structural properties such as the ionic conductivity at elevated temperature⁶, the luminescence^{7,8} and the stabilization of metastable T- ZrO_2 at room temperature. Besides enhancing its photocatalytic activity⁹, oxygen vacancy defects (OVD) were shown to be the origin of ferromagnetism in ZrO_2 nanostructures, making ZrO_2 a promising transparent dilute ferromagnetic semiconductor¹⁰.

While sub-stoichiometric ZrO_{2-x} was produced by high-temperature vacuum techniques, such as pulsed laser deposition¹⁰, the low reducibility of ZrO_2 generally requires drastic post-synthesis treatments like electron or ion irradiation^{11,12}, reduction or evacuation at high temperature¹³ or plasma synthesis⁷ to create OVDs. For sol-gel synthesis, in particular, the amount of non-stoichiometry is usually low and post-treatments, such as the use of an external excitation source (irradiation), thermal treatments in reducing atmosphere or in air, were required to increase the concentration of OVDs^{3,9,14}. However, some of the authors have recently prepared a hybrid ZrO_2 -acetylacetonate material via a hydrolytic sol-gel route that shows absorption of visible light and an unusual catalytic activity for degradation of different organic pollutants in the dark, which was associated with the capability to generate and stabilize the superoxide radical anion on the material surface¹⁵⁻¹⁸. Specifically, it was shown that the presence of acetylacetone lowers the

formation energy of oxygen vacancies, favoring the adsorption of molecular oxygen and its reduction to superoxide¹⁸.

Theoretical calculations for tetragonal^{13,14}, monoclinic¹⁹ and cubic²⁰ zirconia predict OVDs to take the form of F centers, typically observed in non-reducible oxides, where the excess charge stays localized on the vacancy site, even if the partial reduction of the neighboring Zr sites was either not ruled out^{13,20} or specifically considered¹⁴. The formation energy of neutral oxygen vacancies in T-ZrO₂ was predicted to be 6.6 eV using DFT calculations¹³, which is very similar to a neutral F center in MgO (about 7 eV)²¹ and more than 1 eV larger than in more reducible oxides, such as TiO₂¹³. Consequently, the intrinsic defect population in sub-stoichiometric ZrO_{2-x} was interpreted in terms of the following species: F (neutral V_O^{••}); F⁺ (+1 charged V_O[•]), F²⁺ (+2 charged V_O^X), F⁻ (-1 charged V_O^{•••}) and F²⁻ (-2 charged V_O^{••••}) centers^{9,10,13,14,22}. While the existence of Zr³⁺ was shown for materials subjected to the above-mentioned drastic treatments^{5,11,12}, it is not expected to accompany oxygen vacancy formation in a non-reducible oxide. Nevertheless, the presence of Zr³⁺ was invoked in the literature even when the non-stoichiometry was obtained under mild conditions^{14,23-26}. The aforementioned theoretical calculations were however performed using 3x3x2 or 3x3x3 supercells that model a relatively low OVD concentration compared to experiment, making it impossible to conclusively exclude the existence of Zr³⁺ species at higher OVD concentrations.

Here we demonstrate using a combination of experiment and theory that it is possible to obtain sol-gel derived visible light photo-responsive ZrO_{2-x} whose defective structure is characterized by charged oxygen vacancies without Zr³⁺ species. The synergistic control of the processing parameters and post treatments in mild conditions allows achieving a suitable distribution of OVDs. Density functional theory (DFT) calculations performed at the experimental OVD concentration are compared with X-ray photoelectron (XPS), steady state and time-resolved

photoluminescence (PL), as well as ultra-violet and visible light diffuse reflectance (UV-vis-DRS) spectroscopy, to identify OVDs as exclusively neutral or positively charged, which do not give rise to Zr^{3+} species.

XPS analysis of dried and annealed gels. The preparation of metal oxides with cations of high charge/radius ratio (Ti^{4+} , Zr^{4+}) by hydrolytic sol-gel routes requires control of the precursor reactivity to avoid the formation of particulate gels, i.e. gels in which temporary or reversible bonds connect the clusters (physical gels). β -diketones, among them acetylacetonate, were generally used for this purpose as they form very stable metal acetylacetonate complexes $M(acac)_x$ ²⁷. These complexes are retained up to temperatures of about 300 °C in the structure of ZrO_2 and TiO_2 chemical xerogels forming hybrid solids on the surface of which superoxide anion radicals, $O_2^{\bullet-}$, are stably adsorbed^{15-18, 28,29}. Oxygen deficient TiO_{2-x} materials, associated with the formation of Ti^{3+} species, were obtained under reducing synthesis conditions and a large amount of Ti^{3+} self-doping was found in the hybrid gel-derived material annealed in air at 400 °C²⁹. Using a hydrolytic sol-gel route under similar conditions, amorphous white-colored ZrO_2 (SGZ) and hybrid yellow-colored ZrO_2 -acetylacetonate (HSGZ) were obtained. Annealing at 400 °C in air for 1 h transformed these materials into polycrystalline samples formed by nanocrystals dispersed in an amorphous matrix¹⁸. The resulting pure T- ZrO_2 (57% crystallinity degree, mean size of nanocrystals ~23 nm) and almost pure T- ZrO_2 (8% of M- ZrO_2 and 83% crystallinity degree, mean size of nanocrystals ~27 nm) are referred to as HSGZ-400 and SGZ-400, respectively.

The XPS survey spectra (Supplementary Fig. S1) show only Zr and O signals, along with some carbon. In the HSGZ sample the presence of carbon is due to both acac and organic adventitious carbon; the latter is also present in all the other samples, even if its intensity decreases upon annealing. The high resolution XPS spectra of the studied materials are shown in Fig. 1a and the

corresponding binding energy (BE) of the main photoelectron peaks with the kinetic energies of the Zr $M_{45}N_{23}V$ and O KLL X-ray induced Auger lines are listed in Supplementary Table S1. The BE of Zr $3d_{5/2}$ is 182.5 eV, providing evidence that Zr is exclusively present as Zr(IV) in the analysed volume, given that reduced Zr(III) would give rise to peaks at lower BEs. While the Zr 3d signal does not allow to distinguish between Zr-O and Zr-OH that have the same binding energy, the distinction between the associated between O^{2-} and OH^- species can be made from the O1s peaks.

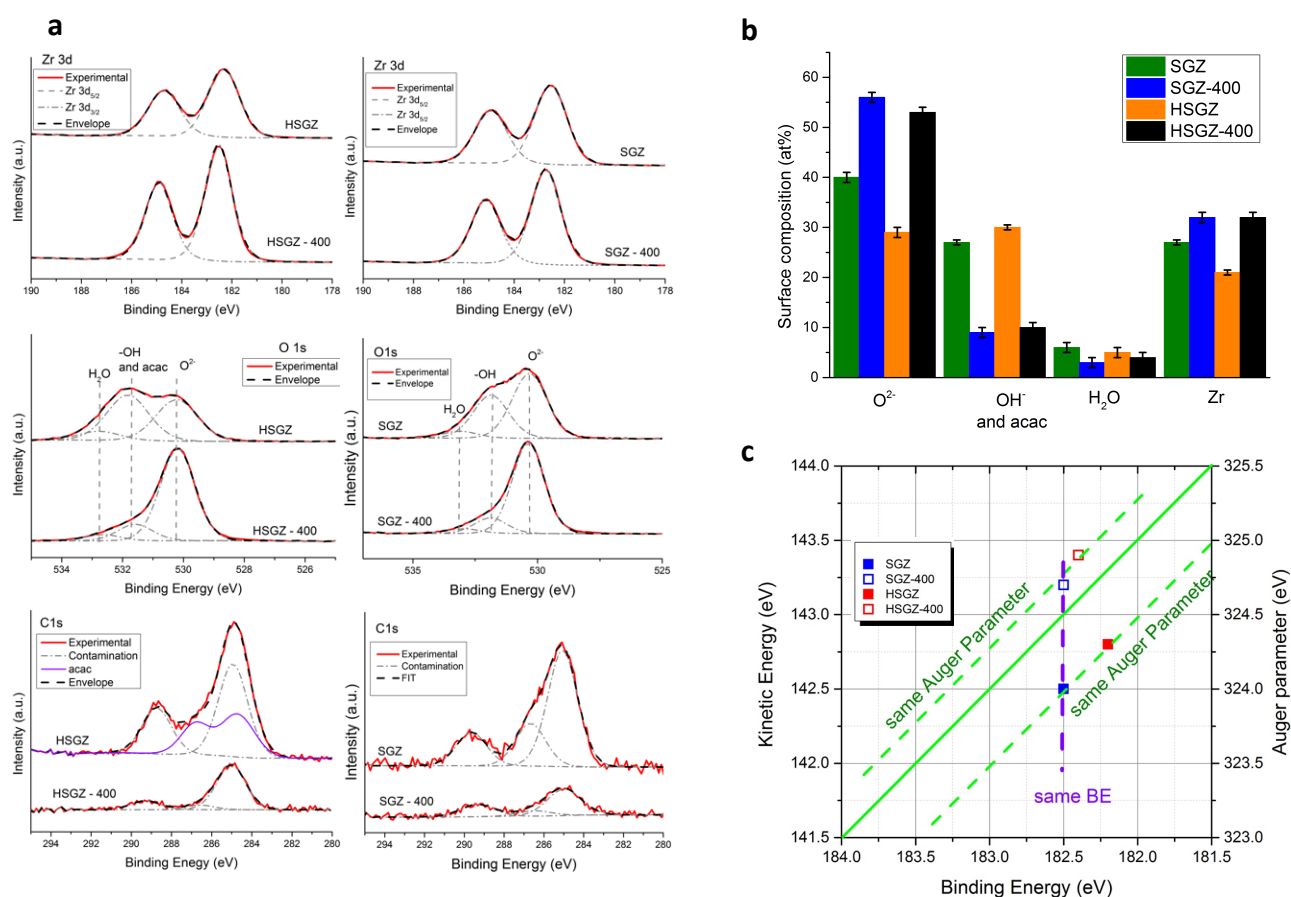


Fig. 1 | XPS characterization. **a.** High resolution Zr 3d, O 1s and C 1s XPS spectra acquired for dried and annealed samples. X-ray source: monochromatic Al $K\alpha$. **b.** Surface composition (at. %) of the analyzed samples after correction for the attenuation due to the presence of a thin carbonaceous contamination layer. The standard deviations are indicated by error bars. **c.** Wagner chemical state plot of zirconium: Zr MNV and Zr 3d; all samples were analyzed in this work.

The atomic concentrations of the different species were evaluated using the areas of the most intense photoelectron peaks. Due to the presence of a thin organic contamination layer (less than

1 nm thick), the electrons of the O1s and Zr 3d signals are attenuated. The electron attenuation depends on the kinetic energy of the emitted electrons and is therefore different for the two elements, given that their BEs are different. To correct for this effect in evaluating the O to Zr atomic ratio, we estimated the thickness of the contamination layer following the approach outlined by Smith³⁰, which relates the thickness of the contamination layer to the percentage of contamination carbon on the sample surface. Once the thickness (d) is estimated, the corrected intensity (I_{corr}) of the Zr and O signals can be calculated from the experimental areas (I_{meas}) by the equation $I_{\text{corr}} = I_{\text{meas}} \exp(d/\lambda \cos\theta)$ where λ is the effective electron attenuation length for photoelectrons in the hydrocarbon overlayer for the element and line of interest and θ is the photoelectron emission angle relative to the surface normal. The corrected compositions expressed as atomic percentages are shown in Fig. 1b, evaluated as a mean over at least three independent measurements. Considering that oxygen is present as O^{2-} , OH^- and C-O or C=O groups of acac molecules, we compute the non-stoichiometry (oxygen deficiency) from the O^{2-} and Zr content. SGZ and HSGZ have the composition $\text{ZrO}_{(2-0.02)}$, SGZ-400 $\text{ZrO}_{(2-0.11)}$ and HSGZ-400 $\text{ZrO}_{(2-0.19)}$. That is, the amorphous samples are almost stoichiometric with $\text{O}/\text{Zr} = 1.98$, while the nanocrystalline ones exhibit higher oxygen defectivity with $\text{O}/\text{Zr} = 1.89$ (SGZ-400) and 1.81 (HSGZ-400).

Since the oxygen content is changing upon heating and higher defectivity is observed in the annealed samples, some effects should be observed on zirconium signals. No evidence of reduced Zr is detected in Zr 3d spectra (Figure 1a), but it is known from literature^{31,32} that the combined use of photoelectron and x-ray induced Auger lines can provide valuable information on the chemical state of elements in different compounds and on the nature of their chemical bonds, especially when no binding energy shift is observed. For this reason, we further investigated the Zr Auger parameter and performed a chemical state plot analysis to clarify if the compositional

changes upon heating are accompanied by any change in the chemical state of zirconium. The modified Auger Parameter (α')^{31,32} is defined as

$$\alpha' = BE_{\text{photoelectron}} + KE_{\text{Auger}} \quad (1)$$

and provides information on the chemical state of an element in different compounds, combining the binding energy of the main photoelectron peak and the kinetic energy of the Auger electrons³³. In Fig. 1c we shown the chemical state plot (or Wagner plot) in which the KE of the Auger electrons (Zr MNV) are plotted versus the BE of the photoelectrons (Zr 3d_{5/2}) for the same element in different compounds. The abscissa is oriented in the negative direction and points for the same element in different compounds falling on green lines (slope: -1) are characterized by the same Auger parameter (α') and have the same chemical state. The point position in the plot depends on initial state effects (local valence charge (q) and Madelung potential (V_M)) and final state effects (extra - atomic relaxation energy R^{ea}, polarizability), the shift in α' representing a simple measurement of the shifts in the extra - atomic relaxation energies: $\Delta\alpha' = \Delta R^{\text{ea}}$. In Fig. 1c, the points belonging to the two dried samples, SGZ and HSGZ fall on a line of slope = -1 and are thus characterized by the same Auger parameter. In this case $\Delta\alpha' = 0$, which by means of $\Delta\alpha' = \Delta BE + \Delta KE$ implies that $\Delta BE = -\Delta KE$. ΔBE and ΔKE , are due to differences in both initial (ΔV) and final state (ΔR^{ea}) effects, in particular:

$$\Delta BE = \Delta V - \Delta R^{\text{ea}} \quad (2)$$

$$\Delta KE = -\Delta V + 3\Delta R^{\text{ea}} \quad (3)$$

But $\Delta R^{\text{ea}} = \Delta\alpha' = 0$, implying that ΔBE and ΔKE observed for the Zr 3d and Zr MNV of the SGZ and HSGZ samples are solely due to initial state effects. Since Zr is only present as Zr(IV) both in SGZ and in HSGZ, the local valence charge is the same and the difference must arise from changes in Madelung potential, that is the potential exerted on Zr atoms by the neighboring atoms. The

presence of the acetylacetonate ligand might be responsible for this difference between the two samples.

The points of the heated samples SGZ-400 and HSGZ-400 fall on a different line, indicating a modification of the chemical state induced by heating. The samples SGZ and SGZ-400 fall on a vertical line (violet line in Fig. 1c), thus $\Delta BE = 0$ (implying by eq. 2 that the initial and final states are similar) and $\Delta\alpha' = \Delta KE$ being positive upon heating. With the constant binding energy of Zr 3d (182.5 eV) the lower Auger parameter for the as received SGZ can directly be interpreted as a more negative Madelung potential experienced by the emitting Zr atom, compared to SGZ-400. Similar results are obtained for HSGZ and HSGZ-400, where small shift in BE of Zr 3d and more intense KE shift of Zr MNV are observed. The more positive Madelung potential for annealed samples can be related to the lower O content, in other words there is evidence of surface non-stoichiometry and an increased oxygen vacancy concentration.

Our XPS analysis therefore rules out the presence of Zr(III), which were previously shown to exist in reduced but fully stoichiometric ZrO_2 ¹⁴, instead providing evidence for a high concentration of OVDs that should lead to F-centers without appearance of Zr(III) species. To ascertain that the electronic structure of OVDs does not change at experimental OVD concentrations and to enable a quantitative comparison of transition energies with our subsequent photoluminescence studies, we perform DFT calculations using a 2x2x2 supercell that better describes the OVD concentration in our samples compared to previous calculations.

Theoretical calculations. The computed bulk density of states (DOS) for stoichiometric and defective tetragonal zirconia is reported in Fig. 2. Tetragonal zirconia belongs to space group $P4_2/nmc$, with eightfold coordinated Zr surrounded by two distorted tetrahedra of O atoms. The computed lattice parameters are $a = 3.58 \text{ \AA}$ and $c = 5.10 \text{ \AA}$, in good agreement with experiment³⁴.

As expected for semi-local GGA functionals, the computed band gap (3.9 eV) is lower than the ones determined experimentally in this work by diffuse reflectance spectroscopy (see below): about 5.1 eV for SGZ-400, a sample with prevalent tetragonal phase, and 5.6 eV for the amorphous SGZ, which agrees with previous reports in the range 5.0 - 5.8 eV for different crystalline phases, synthesis methods and treatments³⁵. The top of the valence band (VB) is mainly formed by O-2*p* states, while Zr-4*d* states dominate the bottom of the conduction band (CB).

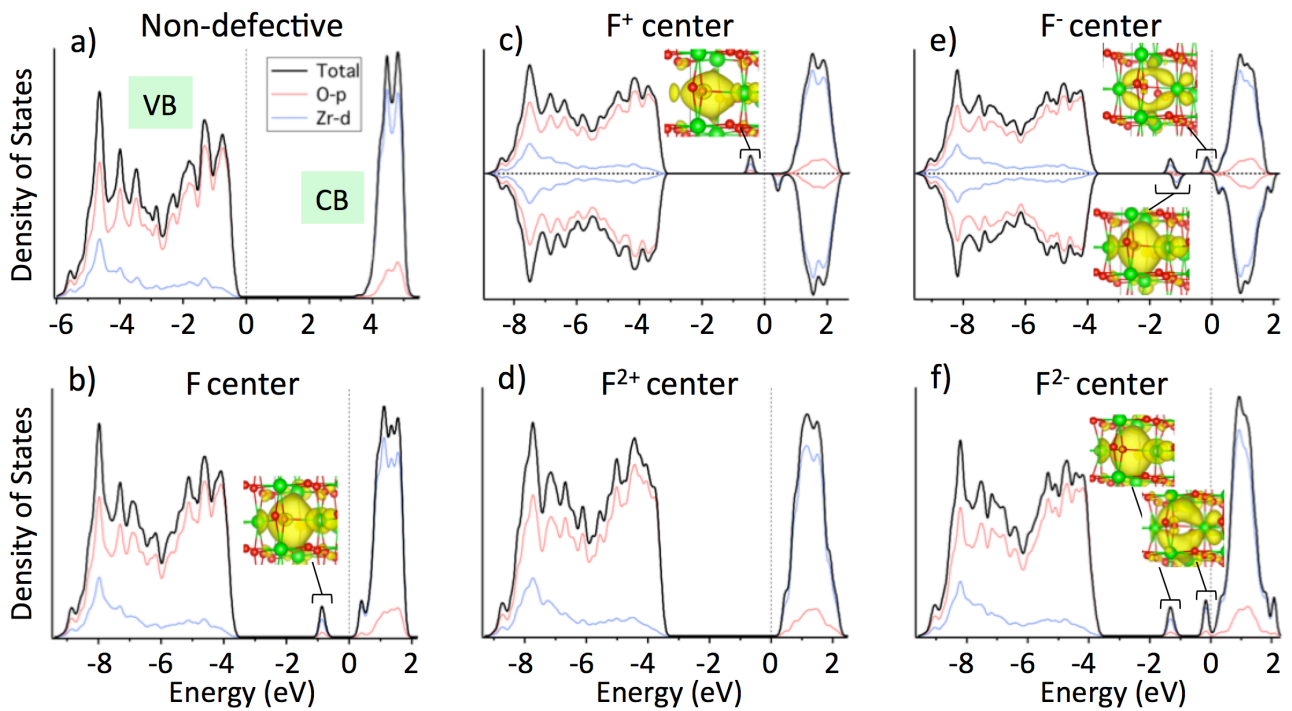


Fig. 2 | DFT calculations. Total and projected density of states (DOS) for the oxygen *p* and zirconium *d* states of **a)** the non-defective T-ZrO₂ bulk structure; **b)** the ZrO₂ supercell with one neutral (F center); **c)** singly positively (F⁺ center); **d)** doubly positively (F²⁺ center); **e)** singly negatively (F⁻ center); **f)** doubly negatively (F²⁻ center) charged oxygen vacancy. The zero of the energy scale is set to the Fermi level. The insets show the integrated local DOS (isosurface values of 0.004 e/Å³) of the highlighted occupied defect states. Zirconium atoms are shown in green and oxygen atoms in red.

Figure 3 reports the formation energy (E_{form}) of the considered OVDs in T-ZrO₂ computed as a function of the Fermi energy (E_{F}), whose range was extended up to the experimental band gap of the SGZ sample (5.6 eV). We note that, despite the underestimation of the band gap, GGA functionals were previously shown to provide a good qualitative description of the properties of

defective zirconia, since the effect of the overestimation of the electron delocalization and the resulting metallic character generally associated with these functionals is not too prominent due to the fairly large band gap of ZrO_2 ²⁰. The formation energy calculated for the neutral oxygen vacancy is 6.5 eV, in line with previous theoretical results^{13,20,36,37}. This high value is an indication of the difficulty of T- ZrO_2 to be reduced, as the concentration of this defect in thermodynamic equilibrium should not be high.

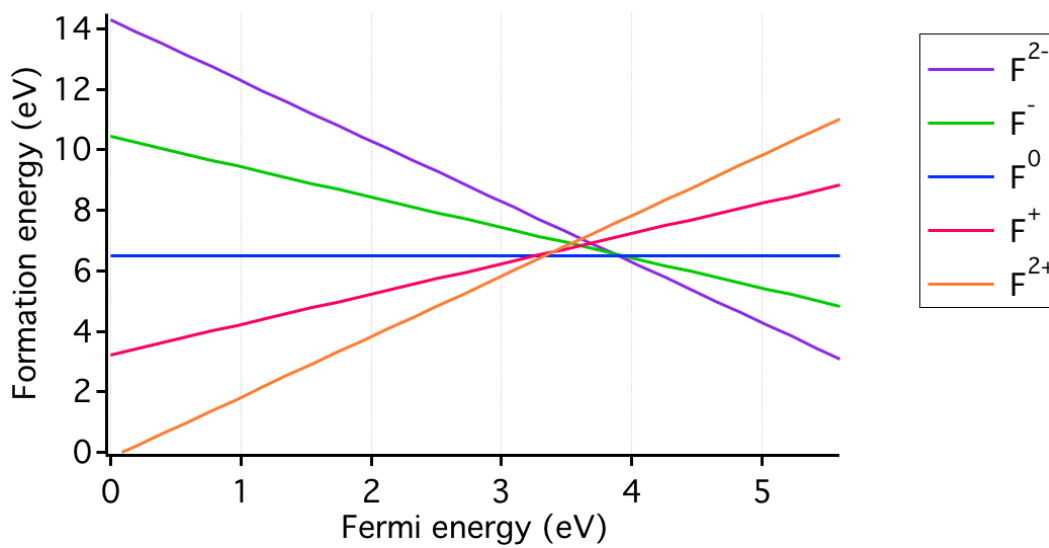


Fig. 3 | Formation energy of OVD. Formation energy as a function of the Fermi energy for oxygen vacancies in different charge states. The range of Fermi energy values is extended up to the experimental band gap of SGZ (5.6 eV).

However, this E_{form} is computed for oxygen rich conditions (*i.e.* oxidizing environment) and should be smaller under the relatively reducing synthesis conditions (presence of organic compounds) of our samples, leading to a higher concentration of OVDs, in line with the experimental observations. We stress here that while this implies that the absolute value for the formation energy will be lower, it does not affect the position of the computed transition levels that we will focus on hereafter.

As expected, with E_F increasing from the valence to the conduction band edge, the minimum-energy defect changes from positively charged, to neutral, and finally negatively charged O

vacancies. The formation energies of F^0 , F^+ , and F^{2+} defects in tetragonal zirconia were calculated in previous work, using a $3 \times 3 \times 2$ super-cell³⁶. Our results differ slightly, most likely due to our smaller supercell, but the defect concentration obtained here is in better agreement with the experimentally determined defect concentration, thus allowing for a more direct comparison. The O to Zr ratio in our case is $31/16 = 1.94$, while that found by XPS is between 1.81 and 1.98 depending on the sample.

When a neutral oxygen atom is removed leaving behind two electrons in the ZrO_2 lattice, a doubly occupied defect state appears in the gap at about 2.8 eV from the VB (see Fig. 2b). The two electrons, previously in O-2p states, now occupy this newly created gap state centered on the vacancy (F-center) with small contributions from Zr-4d states as expected in a non-reducible oxide. If one oxygen atom and one electron are simultaneously removed, a singly positively charged oxygen vacancy (F^+) is obtained. The PDOS in Fig. 2c shows that in this case the defect state is split into two spin components, with a singly occupied spin-up state (at about 2.78 eV from the VB) and an unoccupied spin-down level at the bottom of the CB. Again, the occupied defect state is highly localized on the vacancy site with small contributions on the neighboring Zr atoms. If one electron is removed from the F^+ defect, the F^{2+} -center is created and the now empty defect state merges with the bottom of the CB (Fig. 2d). Strong relaxations (see Table S2) lead to this electronic structure, similarly to what observed for cubic ZrO_2 ³⁸: the DOS of an unrelaxed F^{2+} -center shows an empty defect state in the gap, while the relaxation of the oxygen atoms in NN positions to the vacancy shift this level to the bottom of the CB. We also considered negatively charged O vacancies, corresponding to the case in which additional electrons are trapped in defect states in the gap. For both the F^- (Fig. 2e) and F^{2-} -centers (Fig. 2f), in which one or two additional electrons respectively are trapped in a neutral O vacancy, it is possible to observe two new occupied levels appearing in the gap: the first one at an energy slightly lower than the defect state of the neutral

F-center (at about 2.4 eV from the VB) and the second at about 3.7 eV from the VB. The main difference is that, in the case of the F⁻-center, as a consequence of the odd number of electrons, the doubly occupied defect state is split into two spin-resolved levels that are very close in energy. In both cases, the integrated local density of states associated with the lower-lying defect state (see the inset in Fig. 2e) is similar to the one of the F or F⁺-center, with two electrons trapped in a state that can be described as a vacancy-centered bonding combination of atomic orbitals of the NN Zr atoms. The charge density associated with the defect state close to the CB is instead localized on combinations of states formed from the four Zr ions located around the vacancy, in agreement with what was already reported for F⁻-centers in cubic ZrO₂³⁷.

As summarized in Table S2, the presence of a vacancy causes the nearest oxygen atoms to move closer to the defect, the displacement decreasing going from positively to negatively charged vacancies. The Zr atoms move closer to the vacancy in negatively charged and neutral defects and away from it in the case of the positively charged defects. The general absence of major Zr d contributions to the defect states for neutral and positively charged OVDs is in agreement with the absence of Zr³⁺ in XPS and a further indication for the prevalence of these defect charge states in our samples.

Calculated vs experimental optical transitions. Opposed to previous experimental^{8,39,40} and theoretical^{13,41} studies, we can here perform a direct comparison between the experimental data for pure T-ZrO₂ nanocrystals (HSGZ-400) and the theoretical results since the concentrations of OVDs are comparable. The computed thermodynamic and optical transitions, obtained with equations (S3) and (S4), are displayed in Table 1(a). Thermodynamic transitions (ϵ^{therm}) are representative for long time scales, during which the defect can relax from the equilibrium geometry of the initial charge state to the equilibrium geometry of a different charge state.

Optical transitions (ϵ^{opt}) instead occur on shorter time scales, where a charge-state transition occurs, but the system retains the equilibrium geometry of the initial state. Since optical transitions depend on the charge-transfer direction, we report in Table 1(a) the transitions obtained for both emission and absorption processes. These calculations indicate that F-centers are associated with a series of optical transition levels between 2.08 and 4.19 eV above the VB. The thermodynamic levels are higher in energy than the corresponding optical ones, especially for transition involving singly or doubly positively charged defects, which are associated with larger relaxations of the NN O atoms, as discussed above and shown in Table S2.

The steady-state PL spectra of the different materials, measured using a 325 nm (3.82 eV) exciting laser, are shown in Fig 3a. The excitation wavelength is below the ZrO₂ band-gap and all transitions observed in stationary PL measurements can therefore be attributed to intra-band transitions, involving states in the band gap, which in our samples most likely are OVD-induced F centers.

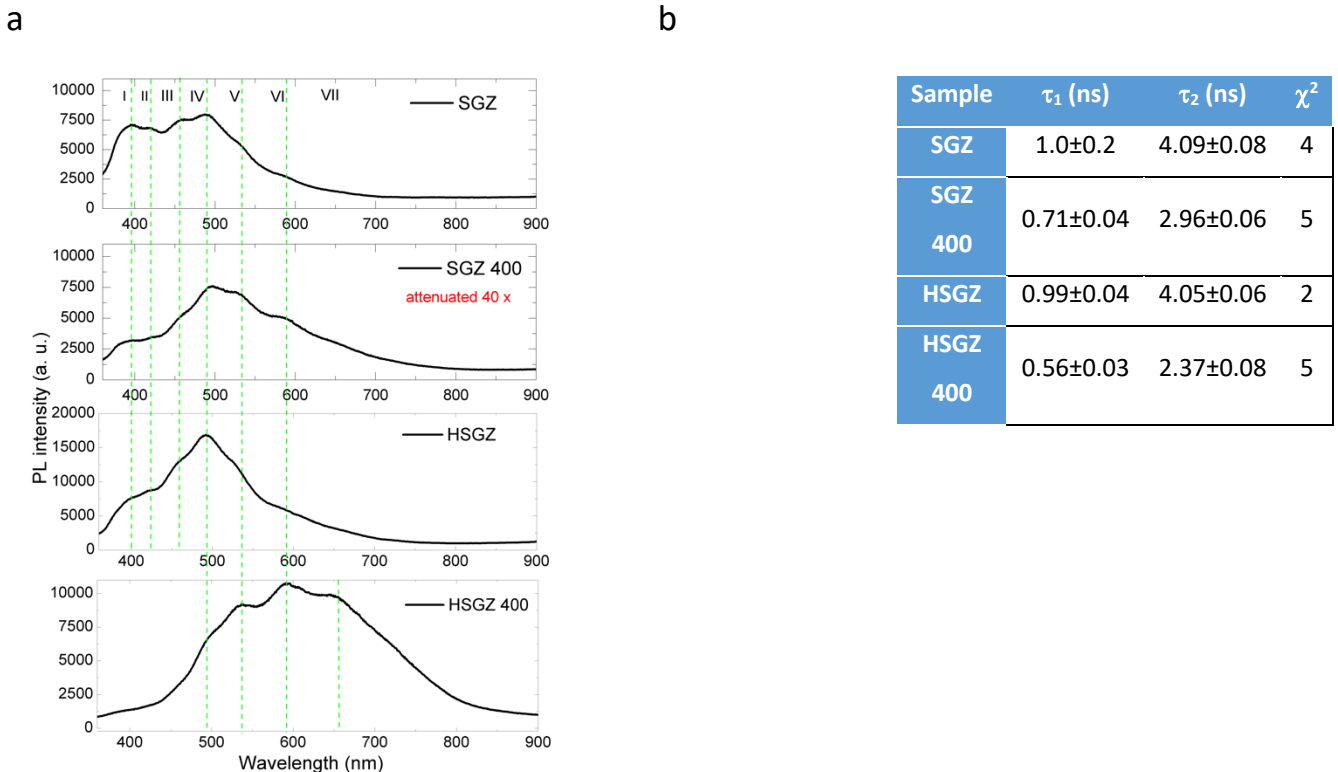


Fig. 3 PL characterization | **a.** Steady-state PL spectra of the studied materials excited at 325 nm. **b.** Fast (τ_1) and slow (τ_2) luminescent lifetimes of samples determined by a bi-exponential model together with χ^2 parameter.

The intense and broad luminescence bands between 649 nm (1.91 eV) and 390 nm (3.17 eV) shown in Fig. 3a result from a set of energy levels, the most prominent peak positions being highlighted by dotted green lines. In our samples, a contribution of carbon-related impurities could be limited to peak I, which is pronounced only in SGZ and HSGZ dried gels and is not present in thermal treated SGZ-400 and HSGZ-400 samples. Thermal annealing at 400 °C, suppresses some of the remaining transitions and creates new ones (i.e., there is not a shift of the PL spectrum, but only intensity changes of individual emission bands). We observe a general increase in luminescence, in particular of peaks V-VII in SGZ-400, which can be attributed to the increased non-stoichiometry after thermal treatment. Due to this result and the above XPS evidence for increased oxygen deficiency, we associate peaks II-VII to OVDs in the ZrO₂ lattice that have different degrees of ionization.

Table 1. Theoretical and experimental transitions | **(a).** Calculated thermodynamic and optical transitions. **(b).** Wavelengths (nm) and energies (eV) of the photoluminescence peaks extracted from PL spectrum fitting. Standard errors are reported in parentheses. For each fit R² was greater than 0.999.

(a)

Transition couple	$\varepsilon^{\text{therm}}$ (eV)	Transition couple	ε^{opt} (eV)	Transition couple	ε^{opt} (eV)
F ²⁻ , F ⁻	3.86	F ²⁻ , F ⁻	3.59	F ⁻ , F ²⁻	4.04
F ²⁻ , F ⁰	3.90	F ²⁻ , F ⁰	3.28	F ⁰ , F ²⁻	4.19
F ⁻ , F ⁰	3.94	F ⁻ , F ⁰	3.62	F ⁰ , F ⁻	4.12
F ⁰ , F ⁺	3.26	F ⁰ , F ⁺	2.72	F ⁺ , F ⁰	3.73
F ⁰ , F ²⁺	3.33	F ⁰ , F ²⁺	2.08	F ²⁺ , F ⁰	4.16
F ⁺ , F ²⁺	3.41	F ⁺ , F ²⁺	2.64	F ²⁺ , F ⁺	4.06

(b)

Sample	Peak 1	Peak 2	Peak 3	Peak 4	Peak 5
SGZ	383 (1) nm	411 (2) nm	451 (2) nm	480 (1) nm	545 (2) nm
	3.24 (0.01) eV	3.02 (0.03) eV	2.75 (0.02) eV	2.58 (0.02) eV	2.28 (0.01) eV
HSGZ	398 (2) nm	476 (2) nm	493 (1) nm	525 (1) nm	556 (2) nm
	3.12 (0.01) eV	2.60 (0.01) eV	2.51 (0.01) eV	2.36 (0.01) eV	2.23 (0.01) eV
SGZ 400	391 (1) nm	-----	493 (1) nm	499 (1) nm	581 (1) nm
	3.17 (0.02) eV		2.51 (0.01) eV	2.48 (0.02) eV	2.13 (0.01) eV
HSGZ 400	400 (1) nm	-----	516 (2) nm	590 (1) nm	627 (2) nm
	3.10 (0.01) eV		2.40 (0.02) eV	2.10 (0.01) eV	1.98 (0.02) eV

For a quantitative comparison with the theoretical results, we fitted the PL spectra using Gaussian functions, choosing the number of functions such as to represent the spectrum with errors smaller than 2% (see Supplementary Figs. S2-S3). The spectra of dried and annealed gels were fitted by five and four Gaussian curves respectively ($R^2 > 0.999$), which may be related to the different degree of crystallinity: HSGZ and SGZ are amorphous, HSGZ-400 and SGZ-400 are nanocrystalline. Since the experimental PL setup contains a pass band filter with the edge at 360 nm (3.44 eV), optical transitions above this value cannot be observed experimentally, which includes for example the vertical decay of one electron from the CB into the neutral defect state (0, -1) predicted at 4.12 eV. Consequently, only the (-2, 0), (0, +1), (0, +2) and (+1, +2) optical transitions that were theoretically computed, can be compared with experimental results. By fitting the PL data the resulting peak positions 1 - 5, reported in Table 1(b), can be related to the theoretically predicted ones in Table 1(a). It can be seen that the fitted peaks are close to the calculated transition energies between neutral or positively ionized defects, confirming the prevalence of these charge states. Quantitative discrepancies between experiment and theory can be ascribed to geometrical effects, i.e. the dimension of the theoretical cell unit, and also the partially amorphous character of the annealed samples: 17% (SGZ-400) and 43% (HSGZ-400). For HSGZ-400, whose structure is closer to the T-ZrO₂ phase used in the calculations than that of SGZ-400, the fitted peaks agree better with the calculations (see Table 1).

Time-resolved PL measurements support the results of the steady-state measurements. Decay constants, extracted from graphs reported in Supplementary Fig. S4, are lower (faster decays) in annealed samples than in dried gels, due to crystallization of the T-ZrO₂ polymorph and the increased number of defects. As can be seen in Fig. 3b, the fast component is in all cases of the order of the detector response time (1 ns), while the slow component (2-4 ns) identifies the nature of the emission centers as F⁺ according to the literature⁴².

The above discussion is consistent with the results of ultra-violet and visible light diffuse reflectance (UV-vis-DRS) spectroscopy. The UV-vis-DRS spectra, calculated using the Kubelka-Munk function $F(R_\infty)$, are displayed in Fig. 4, with images of the samples shown in the inset. All spectra exhibit one or two well-resolved absorption bands except for the light-brown HSGZ-400 that shows a diffuse absorption in the whole UV to visible range. The intensity of each peak was normalized with respect to the O²⁻→Zr⁴⁺ charge transfer transition (i.e. the transition from VB to CB) which for the white colored SGZ occurs at about 200 nm. A progressive red-shift of this band is seen going from about 215 nm (SGZ-400) to about 240 nm (HSGZ-400), associated with the color change of the samples: dark-white (SGZ-400), yellow (HSGZ), light-brown (HSGZ-400) (see inset of Fig. 4). The quantitative evaluation of the optical band gaps (E_g) as well as of the absorption edges was performed by linearization of the plot of $(F(R) \cdot h\nu)^n$ against $h\nu$ where $n=2$ or $n=1/2$ for direct and indirect transitions respectively⁴³. In the studied materials direct transitions occur except for HSGZ, where indirect intraligand transitions take place. The E_g values for SGZ and SGZ-400 are evaluated as 5.65 eV (~ 221 nm) and 5.12 eV (~ 242 nm), respectively. Both of them lie in the UV range and agree well with the two direct band-to-band transitions expected for ZrO₂². The E_g values for HSGZ and HSGZ-400 are 2.55 eV (~ 486 nm) and 2.28 eV (~ 545 nm), respectively, indicating the photoresponsivity to solar light of these materials, which from the above discussion can be ascribed to the presence of OVDs.

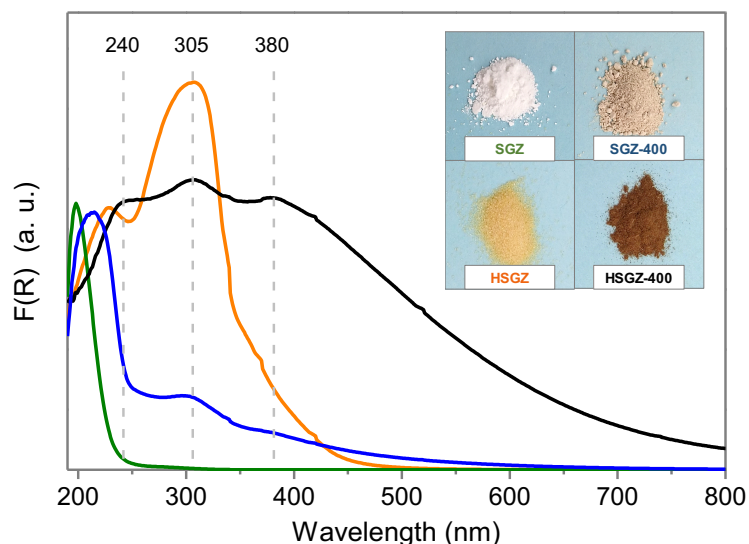


Fig. 4 UV-vis characterization |UV-vis-DRS spectra of the studied materials. In the inset their photos are also displayed.

HSGZ presents a large absorption band with a maximum around 305 nm, a shoulder and a tail in the visible region up to about 550 nm, which can be related to the Zr-acac complex, as shown above by XPS analysis. In particular, it can be assigned to a combined contribution of electronic intraligand transitions ($\pi \rightarrow \pi^*$) with a partial ligand-to-metal charge transfer ($\pi(\text{acac}) \rightarrow \pi^*(\text{acac})/d(\text{Zr})$)¹⁸. On the other hand, a noticeable absorption around the same wavelength is seen in the UV-vis-DRS spectra of both annealed samples. These samples do not contain Zr-acac complexes but as reported above show a marked non-stoichiometry, $\text{ZrO}_{1.89}$ (SGZ-400) and $\text{ZrO}_{1.81}$ (HSGZ-400), with presence of neutral and charged oxygen vacancies. The absence of Zr^{3+} is confirmed by the lack of a characteristic absorption band at 276 nm²² and by a previous electron paramagnetic resonance (EPR) characterization¹⁸. Zr^{3+} is a paramagnetic species with the main component of the axial signal at a g factor about 1.978^{3,25,44}. Such a signal was not detected in the EPR spectra of annealed samples that, instead, exhibited a broad (peak width ~ 5 G) and intense singlet at $g = 2.0024$ ¹⁸. This kind of signal, appearing after thermal treatments of zirconia, has commonly been associated to single electrons trapped in F^+ centers^{3,25,44,45}, representing further

evidence for the presence of this OVD, whereas vacancies with an even number of electrons are diamagnetic and therefore not detectable by EPR.

In conclusion the diffuse visible light absorption in our ZrO_{2-x} samples synthesized under mild reducing condition can be considered to stem from neutral and/or positively charged oxygen vacancies that do not lead to Zr^{3+} species. In particular, for HSGZ-400 the agreement between experiment and theory suggests, that electronic transitions can be assigned to occur between the defect states F^+ and F/F^{2+} that are prevalently present in this sample.

Methods

Synthesis, characterization and computational details with associated references are available in the Supplementary Information.

References

1. Aronne, A.; Marotta, A; Pernice, P; Catauro, M. Sol-gel processing and crystallization of yttria-doped zirconia. *Thermochim. Acta* **275**, 75–82 (1996).
2. Emeline, A. V. & Serpone, N. Relaxation dynamics of processes in colloidal zirconia nanosols. Dependence on excitation energy and temperature. *Chem. Phys. Lett.* **345**, 105–110 (2001).
3. Gionco, C. *et al.* Cerium doped zirconium dioxide as a potential new photocatalytic material. the role of the preparation method on the properties of the material. *Appl. Catal. A Gen.* **504**, 338–343 (2015).
4. Gionco, C. *et al.* Rare earth oxides in zirconium dioxide: How to turn a wide band gap metal oxide into a visible light active photocatalyst. *J. Energy Chem.* **26**, 270–276 (2017).
5. Sinhamahapatra, A., Jeon, J. P., Kang, J., Han, B. & Yu, J. S. Oxygen-Deficient Zirconia (ZrO_{2-x}): A New Material for Solar Light Absorption. *Sci. Rep.* **6**, 1–8 (2016).
6. Goff, J. P., Hayes, W., Hull, S., Hutchings, M. T. & Clausen, K. N. Defect structure of yttria-

stabilized zirconia and its influence on the ionic conductivity at elevated temperatures.

Phys. Rev. B **59**, 14202–14219 (1999).

7. Smits, K. *et al.* Intrinsic defect related luminescence in ZrO₂. *J. Lumin.* **131**, 2058–2062 (2011).
8. Cong, Y., Li, B., Yue, S., Fan, D. & Wang, X. Effect of Oxygen Vacancy on Phase Transition and Photoluminescence Properties of Nanocrystalline Zirconia Synthesized by the One-Pot Reaction. *J. Phys. Chem. C* **113**, 13974–13978 (2009).
9. Kumar, S. & Ojha, A. K. Oxygen vacancy induced photoluminescence properties and enhanced photocatalytic activity of ferromagnetic ZrO₂ nanostructures on methylene blue dye under ultra-violet radiation. *J. Alloys Compd.* **644**, 654–662 (2015).
10. Rahman, M. A., Rout, S., Thomas, J. P., McGillivray, D. & Leung, K. T. Defect-Rich Dopant-Free ZrO₂ Nanostructures with Superior Dilute Ferromagnetic Semiconductor Properties. *J. Am. Chem. Soc.* **138**, 11896–11906 (2016).
11. Costantini, J. M., Beuneu, F., Morrison-Smith, S., Devanathan, R. & Weber, W. J. Paramagnetic defects in electron-irradiated yttria-stabilized zirconia: Effect of yttria content. *J. Appl. Phys.* **110**, (2011).
12. Costantini, J. M. *et al.* Colour centre production in yttria-stabilized zirconia by swift charged particle irradiations. *J. Phys. Condens. Matter* **16**, 3957–3971 (2004).
13. Gerosa, M. *et al.* Defect calculations in semiconductors through a dielectric-dependent hybrid DFT functional: The case of oxygen vacancies in metal oxides. *J. Chem. Phys.* **143**, 1–11 (2015).
14. Gionco, C. *et al.* Paramagnetic defects in polycrystalline zirconia: An EPR and DFT study. *Chem. Mater.* **25**, 2243–2253 (2013).
15. Aronne, A. *et al.* Use of a new hybrid sol-gel zirconia matrix in the removal of the herbicide

- MCPA: A sorption/degradation process. *Environ. Sci. Technol.* **46**, 1755–1763 (2012).
16. Sannino, F., Pirozzi, D., Vitiello, G. & Gerardo, D. Oxidative degradation of phenanthrene in the absence of light irradiation by hybrid ZrO₂-acetylacetonate gel-derived catalyst. *Appl. Catal. B Environ.* **156–157**, 101–107 (2014).
 17. Sannino, F. *et al.* Oxidative Degradation of Different Chlorinated Phenoxyalkanoic Acid Herbicides by a Hybrid ZrO₂ Gel-Derived Catalyst without Light Irradiation. (2015).
 18. Muñoz-García, A. B. *et al.* Origin and Electronic Features of Reactive Oxygen Species at Hybrid Zirconia-Acetylacetonate Interfaces. *ACS Appl. Mater. Interfaces* **7**, 21662–21667 (2015).
 19. Lopez Gejo, F., Foster, A. S., Nieminen, R. M., Shluger, A. L. & Sulimov, V. B. Structure and electrical levels of point defects in monoclinic zirconia. *Phys. Rev. B - Condens. Matter Mater. Phys.* **64**, 1–10 (2001).
 20. Ganduglia-Pirovano, M. V., Hofmann, A. & Sauer, J. Oxygen vacancies in transition metal and rare earth oxides: Current state of understanding and remaining challenges. *Surf. Sci. Rep.* **62**, 219–270 (2007).
 21. Pacchioni, G. Defects at Oxide Surface. in *Springer Series in Surface Science* 1–28 (2015).
 22. Emeline, A. *et al.* Spectroscopic and Photoluminescence Studies of a Wide Band Gap Insulating Material: Powdered and Colloidal ZrO₂ Sols. *Langmuir* **14**, 5011–5022 (1998).
 23. Liu, H., Feng, L., Zhang, X. & Xue, Q. ESR Characterization of ZrO₂ Nanopowder. *J. Phys. Chem.* **99**, 332–334 (1995).
 24. Lakshmi, J. S., John Berlin, I., Daniel, G. P., Thomas, P. V. & Joy, K. Effect of calcination atmosphere on photoluminescence properties of nanocrystalline ZrO₂ thin films prepared by sol-gel dip coating method. *Phys. B Condens. Matter* **406**, 3050–3055 (2011).
 25. Matta, J., Lamonier, J. F., Abi-Aad, E., Zhilinskaya, E. A. & Aboukaïs, A. Transformation of

- tetragonal zirconia phase to monoclinic phase in the presence of Fe³⁺ ions as probes: An EPR study. *Phys. Chem. Chem. Phys.* **1**, 4975–4980 (1999).
26. Zhao, Q., Wang, X. & Cai, T. The study of surface properties of ZrO₂. *Appl. Surf. Sci.* **225**, 7–13 (2004).
 27. Schubert, U. Organically modified transition metal alkoxides: Chemical problems and structural issues on the way to materials syntheses. *Acc. Chem. Res.* **40**, 730–737 (2007).
 28. Sannino, F. *et al.* Hybrid TiO₂-acetylacetonate amorphous gel-derived material with stably adsorbed superoxide radical active in oxidative degradation of organic pollutants. *RSC Adv.* **5**, 93831–93839 (2015).
 29. Aronne, A. *et al.* Electronic properties of TiO₂-based materials characterized by high Ti³⁺ self-doping and low recombination rate of electron-hole pairs. *RSC Adv.* **7**, 2373–2381 (2017).
 30. Smith, G. C. Evaluation of a simple correction for the hydrocarbon contamination layer in quantitative surface analysis by XPS. *J. Electron Spectros. Relat. Phenomena* **148**, 21–28 (2005).
 31. Wagner, C. D., Gale, L. H. & Raymond, R. H. Two-Dimensional Chemical State Plots: a Standardized Data Set for Use in Identifying Chemical States By X-Ray Photoelectron Spectroscopy. *Anal Chem* **51**, 466–482 (1979).
 32. Moretti, G. Auger parameter and Wagner plot in the characterization of chemical states by X-ray photoelectron spectroscopy: a review. *J. Electron Spectros. Relat. Phenomena* **95**, 95–144 (1998).
 33. Cocco, F., Elsener, B., Fantauzzi, M., Atzei, D. & Rossi, A. Nanosized surface films on brass alloys by XPS and XAES. *RSC Adv.* **6**, 31277–31289 (2016).
 34. Teufer, G. The crystal structure of tetragonal ZrO₂. *Acta Crystallogr.* **15**, 1187–1187 (1962).

35. Kumari, L. *et al.* Controlled Hydrothermal Synthesis of Zirconium Oxide Nanostructures and Their Optical Properties. *Cryst. Growth Des.* **9**, 3874–3880 (2009).
36. Eichler, A. Tetragonal Y-doped zirconia: Structure and ion conductivity. *Phys. Rev. B - Condens. Matter Mater. Phys.* **64**, 1–8 (2001).
37. Gionco, C. *et al.* Cerium-doped zirconium dioxide, a visible-light-sensitive photoactive material of third generation. *J. Phys. Chem. Lett.* **5**, 447–451 (2014).
38. Stapper, G., Bernasconi, M., Nicoloso, N. & Parrinello, M. Ab initio study of structural and electronic properties of yttria-stabilized cubic zirconia. *Phys. Rev. B* **59**, 797–810 (1999).
39. Lin, C., Zhang, C. & Lin, J. Phase Transformation and Photoluminescence Properties of Nanocrystalline ZrO₂ Powders Prepared via the Pechini-type Sol - Gel Process. *J. Phys. Chem C* **111**, 3300–3307 (2007).
40. Smits, K., Grigorjeva, L., Łojkowski, W. & Fidelus, J. D. Luminescence of oxygen related defects in zirconia nanocrystals. *Phys. Status Solidi Curr. Top. Solid State Phys.* **4**, 770–773 (2007).
41. French, R. H., Glass, S. J., Ohuchi, F. S., Xu, Y. & Ching, W. Y. Experimental and theoretical determination of the electronic structure and optical properties of three phases of ZrO₂. *Phys Rev B Condens Matter* **49**, 5133–5142 (1994).
42. Aleksanyan, E., Kirm, M., Feldbach, E. & Harutyunyan, V. Identification of F⁺ centers in hafnia and zirconia nanopowders. *Radiat. Meas.* **90**, 84–89 (2015).
43. Addonizio, Maria, L. *et al.* Sol – gel synthesis of ZnO transparent conductive films : The role of pH. *Appl. Surf. Sci.* **305**, 194–202 (2014).
44. Bobricheva, V. *et al.* R study of paramagnetic sites in sulfated zirconia. *Catal. Letters* **56**, 23–27 (1998).
45. Occhiuzzi, M., Cordischi, D. & Dragone, R. Intrinsic and extrinsic paramagnetic centers in

zirconia. *J. Phys. Chem. B* **106**, 12464–12469 (2002).